Journal of the Taiwan Institute of Chemical Engineers 45 (2014) 1892–1909

Contents lists available at ScienceDirect

Journal of the Taiwan Institute of Chemical Engineers

journal homepage: www.elsevier.com/locate/jtice

Controlled hydrothermal synthesis of bismuth oxybromides and their photocatalytic properties

Hong-Lin Chen [a], Wenlian William Lee [b,c], Wen-Hsin Chung [d], Ho-Pan Lin [a], Yen-Ju Chen [a], Yu-Rou Jiang [a], Wan-Yu Lin [d], Chiing-Chang Chen [a,*]

[a] Department of Science Application and Dissemination, National Taichung University of Education, Taichung 403, Taiwan, ROC
[b] Department of Occupational Safety and Health, Chung-Shan Medical University, Taichung 402, Taiwan, ROC
[c] Department of Occupational Medicine, Chung Shan Medical University Hospital, Taichung 402, Taiwan, ROC
[d] Department of Plant Pathology, National Chung Hsing University, Taichung 402, Taiwan, ROC

ARTICLE INFO

Article history:
Received 13 August 2013
Received in revised form 12 November 2013
Accepted 14 December 2013
Available online 7 January 2014

Keywords:
Bismuth oxybromide
Autoclave hydrothermal
Visible-light-responsive photocatalyst

ABSTRACT

Ternary bismuth oxybromides have been synthesized using autoclave hydrothermal methods. The products are characterized by XRD, SEM–EDS, XPS, FTIR, and DRS. We demonstrate that $Bi_{12}O_{17}Br_2$, Bi_5O_7Br, Bi_3O_4Br, $Bi_{24}O_{31}Br_{10}$, $Bi_4O_5Br_2$, and BiOBr can be selectively prepared through a facile solution-based hydrothermal method. UV–vis spectra show bismuth oxybromide materials to be indirect semiconductors with an optical band gap of 2.22–2.76 eV. Photocatalytic efficiencies of powder suspensions were evaluated by measuring the Crystal Violet (CV) concentration. This is the first study to show the superior activities of $Bi_{12}O_{17}Br_2$, Bi_5O_7Br, Bi_3O_4Br, and $Bi_4O_5Br_2$ as a promising visible-light-responsive photocatalyst.

1. Introduction

Heterogeneous photocatalysis for environmental remediation and solar energy conversion has aroused extensive interest in the past decade. For the practical application of photocatalysis, an environmentally sturdy and inexpensive photocatalyst is an important component [1]. Among the various photocatalytic materials, nano-scaled TiO_2 is studied most, however, it can only be activated by irradiation under UV, which contains less than 5% of the solar spectrum [2]. To utilize visible light and harvest solar energy efficiently, intensive efforts have attempted to develop visible-light-responsive photocatalysts, such as metal/nonmetal doped TiO_2 [3], inorganic bismuth compounds (Bi_2WO_6 [4], Bi_2MoO_6 [5] and $BiVO_4$ [6]), and ferrites [7]. Although most photocatalysts show markedly visible-light-responsive activity, their stabilities, the relationship between structure and photocatalytic reactivity, and photocatalysis mechanisms remain uncertain [8]. Therefore, synthesizing novel visible-light-responsive photocatalysts [9–11] and exploring their photocatalysis performance are of great interest and potential award [12].

Among the bismuth oxyhalides [13], bismuth oxybromides have received remarkable attention in recent years because of their stability, suitable band gaps, and relatively superior photocatalytic abilities [14–17]. BiOBr flakes showed superior photocatalytic abilities than P25-TiO_2 in degrading dyes under visible light (>400 nm) illumination [18]. The Fang group synthesized BiOBr by hydrothermal methods, which exhibited excellent photocatalytic efficiency and good stability during microcystin-LR photodegradation under visible light irradiation [19]. Li et al. recently reported a facile, hydrothermal synthetic pathway for preparing single-crystalline nano-belts of bismuth oxyhalides [20].

Triphenylmethane dyes are used extensively in the textile industry for dyeing nylon, wool, cotton, and silk, as well as for coloring of oil, fats, waxes, varnish, and plastics. The paper, leather, cosmetic, and food industries consume a high quantity of triphenylmethane dyes of various kinds [21]. Cationic triphenylmethane dyes have found widespread use as colorants in industry and as antimicrobial agents [22]. Recent reports indicate that they may further serve as targetable sensitizers in the photo-destruction of specific cellular components or cells [23]. CV is a basic triphenylmethane-type cationic dye, usually used for staining solutions in medicine and biology [24] and as a photochromophore to sensitize gelatinous films [25]. It has been used to differentiate between deoxyribonucleic acid and ribonucleic acid [26]. The binding of CV to DNA is probably ionic, as opposed to intercalative, and it remains so stably bound to double-stranded DNA that, with its conversion to the colorless carbinol from, it has been used to assess the binding of other molecules to DNA [27]. However, great concern has arisen about the thyroid peroxidase-catalyzed

* Corresponding author. Tel.: +886 4 2218 3406; fax: +886 4 2218 3560.
E-mail addresses: ccchen@mail.ntcu.edu.tw, ccchen@ms3.ntcu.edu.tw (C.-C. Chen).

1876-1070/$ – see front matter © 2013 Taiwan Institute of Chemical Engineers. Published by Elsevier B.V. All rights reserved.
http://dx.doi.org/10.1016/j.jtice.2013.12.015

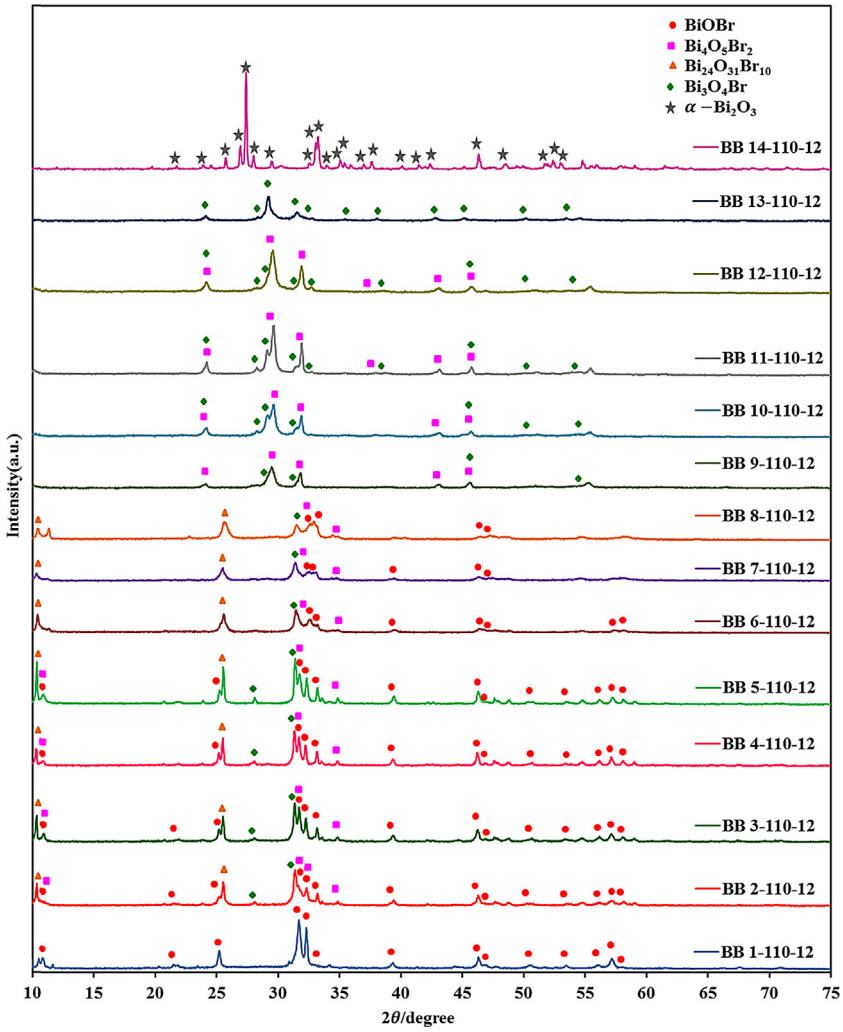

Fig. 1. XRD patterns of as-prepared powders under different pH value, at reaction temperature 110 °C and reaction times 12 h.

oxidation of the triphenylmethane class of dyes because the reactions might form various *N*-de-alkylated primary and secondary aromatic amines, with structures similar to aromatic amine carcinogens [28].

In early reports [29–32], most studies focused on bismuth oxyiodides, not on bismuth oxybromides under visible-light irradiation. Reports in the literature [33,34] on the photocatalytic degradation of triphenylmethane dyes under visible light or sunlight are few. They examined the effects of various parameters like the initial concentration of substrates, amount of catalysts, and pH values. However, the mechanisms of the bismuth oxybromides-assisted photocatalytic degradation of triphenylmethane dye under visible light irradiation have never been reported.

To the best of our knowledge, photocatalytic degradation of organic pollutants by $Bi_{12}O_{17}Br_2$, Bi_5O_7Br, Bi_3O_4Br, and $Bi_4O_5Br_2$ have not been documented in the literature. This study synthesized $Bi_{12}O_{17}Br_2$, Bi_5O_7Br, Bi_3O_4Br, $Bi_{24}O_{31}Br_{10}$, $Bi_4O_5Br_2$, and BiOBr studied their photocatalytic ability for removing CV in aqueous solutions under visible-light irradiation.

Table 1
Bismuth oxybromides obtained under different reaction conditions.

pH	*T* (°C)/*t* (h)			
	110 °C/12 h	160 °C/12 h	210 °C/12 h	260 °C/12 h
1	BB 1-110-12	BB 1-160-12	BB 1-210-12	BB 1-260-12
2	BB 2-110-12	BB 2-160-12	BB 2-210-12	BB 2-260-12
3	BB 3-110-12	BB 3-160-12	BB 3-210-12	BB 3-260-12
4	BB 4-110-12	BB 4-160-12	BB 4-210-12	BB 4-260-12
5	BB 5-110-12	BB 5-160-12	BB 5-210-12	BB 5-260-12
6	BB 6-110-12	BB 6-160-12	BB 6-210-12	BB 6-260-12
7	BB 7-110-12	BB 7-160-12	BB 7-210-12	BB 7-260-12
8	BB 8-110-12	BB 8-160-12	BB 8-210-12	BB 8-260-12
9	BB 9-110-12	BB 9-160-12	BB 9-210-12	BB 9-260-12
10	BB 10-110-12	BB 10-160-12	BB 10-210-12	BB 10-260-12
11	BB 11-110-12	BB 11-160-12	BB 11-210-12	BB 11-260-12
12	BB 12-110-12	BB 12-160-12	BB 12-210-12	BB 12-260-12
13	BB 13-110-12	BB 13-160-12	BB 13-210-12	BB 13-260-12
14	BB 14-110-12	BB 14-160-12	BB 14-210-12	BB 14-260-12

2. Experimental

2.1. Materials

The purchased $Bi(NO_3)_3{\cdot}5H_2O$, CV dye (TCI), and KBr (Katayama) were obtained and used without any further purification. Reagent-grade HNO_3, NaOH, CH_3COONH_4, and HPLC-grade methanol were obtained from Merck. The de-ionized water used in this study was purified with a Milli-Q water ion-exchange system for a resistivity of $1.8 \times 10^7\ \Omega$ cm.

2.2. Synthesis of bismuth oxybromide

5 mmol of $Bi(NO_3)_3{\cdot}5H_2O$ were first mixed in a 100 mL flask, followed by adding 5 mL of 4 M HNO_3. With continuous stirring, 2 M of NaOH were added dropwise to adjust the pH value to 1–14 and when a white precipitate was formed, then 2 mL of KBr were also added dropwise. The solution was then stirred vigorously for 30 min and transferred into a 30 mL Teflon-lined autoclave, which was heated to 60–280 °C for 12, 24, and 36 h and then naturally cooled to room temperature. The resulting solid product was collected by filtration, then washed with deionized water and methanol to remove any possible ionic species in the product, and then dried at 60 °C overnight. The samples are listed in Table 1.

2.3. Characterization

The precipitates were further characterized. XRD was performed on a MAC Science, MXP18 X-ray diffractometer with Cu Kα radiation, and operated at 40 kV and 80 mA. FE-SEM–EDS measurements were carried out with a field-emission microscope (JEOL JSM-7401F) at an acceleration voltage of 15 kV and an HRXPS measurement was conducted with ULVAC-PHI XPS. The Al Kα radiation was generated with a voltage of 15 kV. Absorption measurements were conducted using a Shimadzu UV-2100S spectrophotometer. The HPLC–PDA–ESI-MS system consisted of a Waters 1525 binary pump, a 2998 photodiode array detector, and a 717 plus autosampler.

2.4. Photocatalytic reaction

Photocatalytic activities of bismuth oxybromides were studied by degrading CV under visible light irradiation of a 20 W lamp. An average irradiation intensity of 5.2 W/m^2 was maintained throughout the experiments and was measured by internal radiometer. Aqueous dispensions of CV (100 mL, 10 ppm) and the given amount of catalyst powder were placed in a Pyrex flask. The pH value of the dispension was adjusted by adding either NaOH or HNO_3 solutions. Before irradiation, the dispensions were magnetically stirred in the dark for 30 min to reach an adsorption/desorption equilibrium between the dye and the catalyst surface under ambient air-equilibrated conditions. At the given irradiation time intervals, 5 mL of aliquot were collected and centrifuged to remove the catalyst. The supernatant was analyzed by HPLC–ESI-MS after readjusting the chromatographic conditions to make the mobile phase compatible with the working conditions of the mass spectrometer.

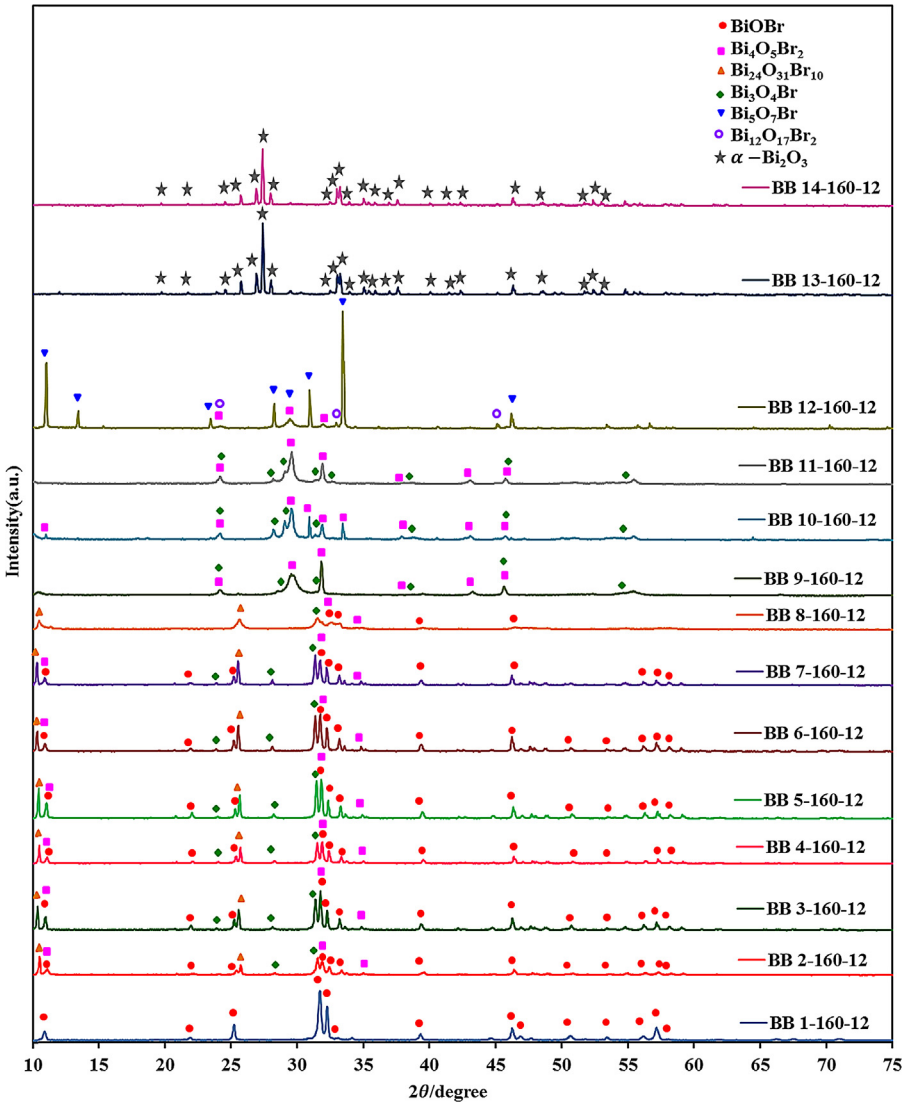

Fig. 2. XRD patterns of as-prepared powders under different pH value, at reaction temperature 160 °C and reaction times 12 h.

3. Results and discussion

3.1. Characterizations of as-prepared powders

3.1.1. XRD analysis

The X-ray diffraction data of bismuth oxybromide samples prepared with different hydrothermal parameters are shown in Figs. 1–4. Figs. 1–4 show X-ray diffraction data for bismuth oxybromide samples prepared at pH = 1–14, 12 h and for 110 °C, 160 °C, 210 °C, and 260 °C, respectively. Table 2 summarizes the results of the XRD measurements. XRD patters clearly revealed the existence pure phase and the coexistence of the different phases. All the bismuth oxybromide samples synthesized using the hydrothermal method described at different temperatures and pH are the BiOBr (JCPDS 09-0393), $Bi_4O_5Br_2$ (JCPDS 37-0669), $Bi_{24}O_{31}Br_{10}$ (JCPDS 75-0888), Bi_3O_4Br (JCPDS 84-0793), Bi_5O_7Br (JCPDS 38-0493), $Bi_{12}O_{17}Br_2$ (JCPDS 37-0701), and α-Bi_2O_3 (JCPDS 41-1449) phase.

The pH of a reaction is generally accepted to have great influence on determining the composition and morphologies of the final products [20]. Control experiments have been conducted to investigate the influence of pH on the reaction. In our experiment, pH plays a key role in controlling the composition and anisotropic growth of crystals. From the results listed in Table 2, the controllable crystal phases and morphologies of bismuth oxybromide could be achieved by simply changing some growth parameters, including pH and temperature. Normally, BiOBr was acquired at pH ≦ 8 and pure phase BiOBr at pH = 1, temp = 110–160 °C; $Bi_4O_5Br_2$ between pH ≧ 1, temp ≧ 210 °C and pH ≦ 12, temp ≦ 160 °C; $Bi_{24}O_{31}Br_{10}$ between pH ≧ 1, temp ≧ 210 °C and pH ≦ 9, temp ≧ 210 °C; Bi_3O_4Br between pH ≦ 1, temp ≧ 210 °C and pH ≦ 12, temp ≦ 110 °C and pure phase Bi_3O_4Br at pH = 13, temp = 110 °C; Bi_5O_7Br between pH ≧ 10, temp ≧ 210 °C and pH ≦ 12, temp ≦ 210 °C; $Bi_{12}O_{17}Br_2$ at pH = 12 and 160 °C ≦ temp ≦ 260 °C and pure phase $Bi_{12}O_{17}Br_2$ at 260 °C; and, Bi_2O_3 microstructures at higher base concentration (pH ≧ 13) in the synthetic conditions. The possible processes for the formation of bismuth oxybromides are described as follows [Eqs. (1)–(10)]:

$$Bi^{3+} + 3OH^- \rightarrow Bi(OH)_{3(s)} \quad (1)$$

$$2Bi(OH)_{3(s)} + Br^- \rightarrow BiOBr_{(s)} + H_2O + OH^- \quad (2)$$

$$Bi^{3+} + 3Br^- \rightarrow BiBr_{3(s)} \quad (3)$$

$$BiBr_{3(s)} + 2OH^- \rightarrow BiOBr_{(s)} + 2Br^- + H_2O \quad (4)$$

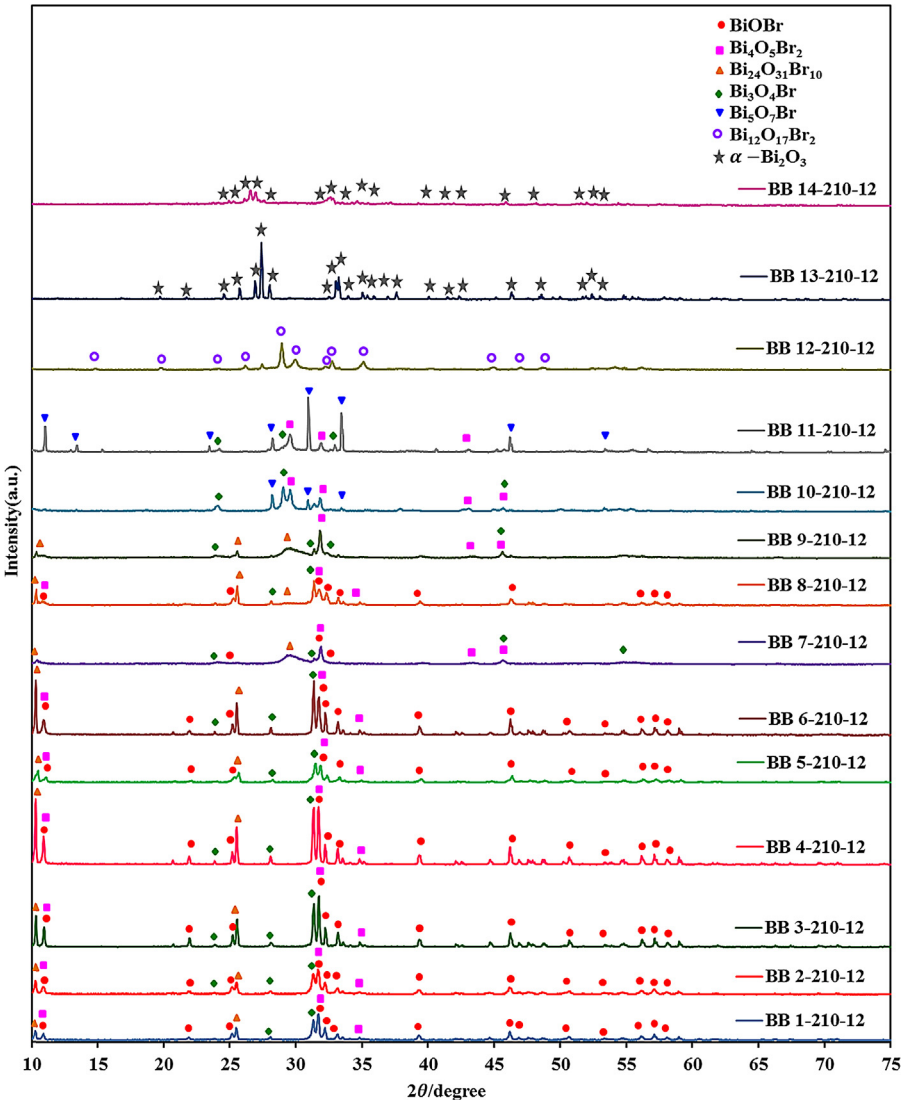

Fig. 3. XRD patterns of as-prepared powders under different pH value, at reaction temperature 210 °C and reaction times 12 h.

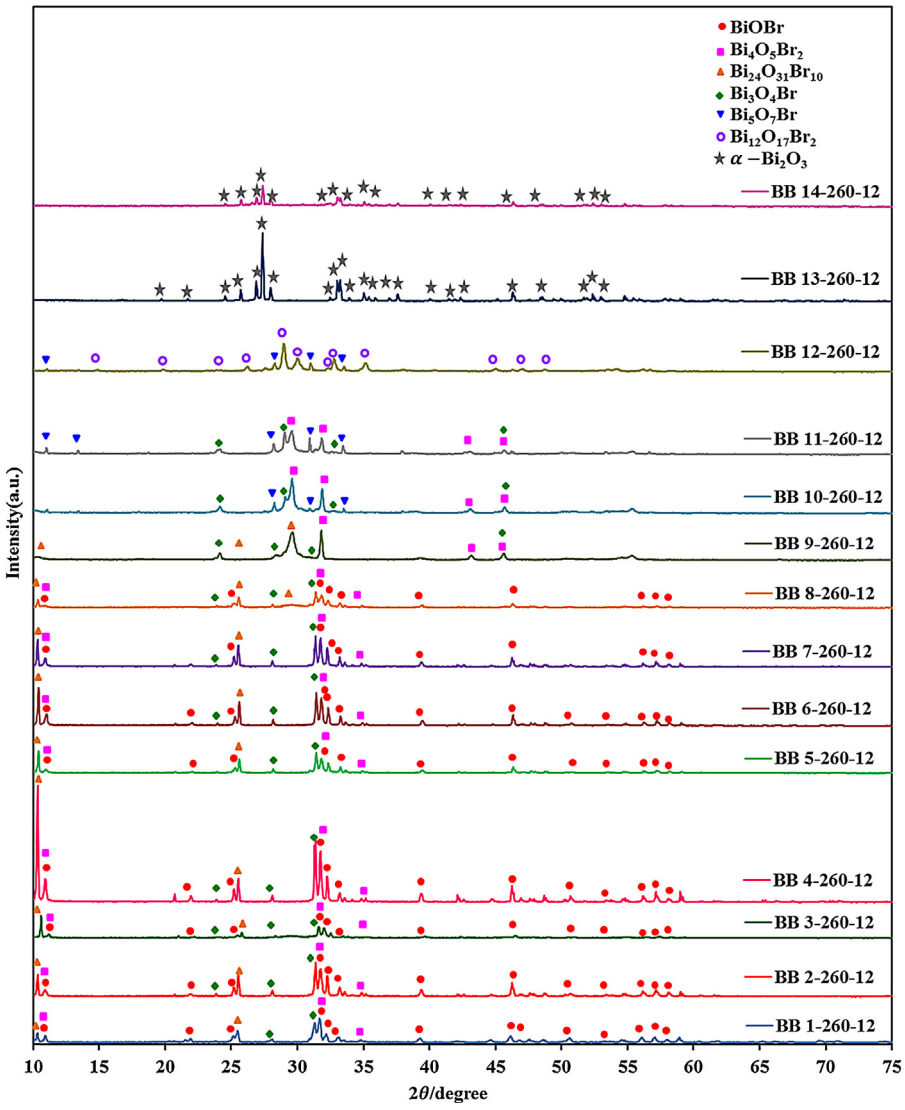

Fig. 4. XRD patterns of as-prepared powders under different pH value, at reaction temperature 260 °C and reaction times 12 h.

$$4BiOBr_{(s)} + 2OH^- \rightarrow Bi_4O_5Br_{2(s)} + 2Br^- + H_2O \quad (5)$$

$$6Bi_4O_5Br_{2(s)} + 2OH^- \rightarrow Bi_{24}O_{31}Br_{10(s)} + 2Br^- + H_2O \quad (6)$$

$$Bi_{24}O_{31}Br_{10(s)} + 2OH^- \rightarrow 8Bi_3O_4Br_{(s)} + 2Br^- + H_2O \quad (7)$$

$$5Bi_3O_4Br_{(s)} + 2OH^- \rightarrow 3Bi_5O_7Br_{(s)} + 2Br^- + H_2O \quad (8)$$

$$12Bi_5O_7Br_{(s)} + 2OH^- \rightarrow 5Bi_{12}O_{17}Br_{2(s)} + 2Br^- + H_2O \quad (9)$$

$$Bi_{12}O_{17}Br_{2(s)} + 2OH^- \rightarrow 6Bi_2O_{3(s)} + 2Br^- + H_2O \quad (10)$$

These equations show that BiOBr was formed at the beginning of the reaction, then OH^- gradually substituted Br^- in the basic conditions, which resulted in the reduced content of Br^- in the products. Increasing the pH gradually obtained $Bi_4O_5Br_2$, $Bi_{24}O_{31}Br_{10}$, Bi_3O_4Br, Bi_5O_7Br, $Bi_{12}O_{17}Br_2$, and α-Bi_2O_3. The higher the pH value, the lower the Br^- content in the products, until the content of Br^- in the products was fully replaced by OH^-, finally resulting in the formation of α-Bi_2O_3 under strong basic conditions. However, BiOBr is the exclusive product at pH 1. A competitive relationship typically exists between the OH^- and Br^- ions in basic solution. By controlling the pH of the reaction, different compositions of bismuth oxybromide were obtained.

It is found that with the increase of hydrothermal temperature range from 110 to 260 °C a gradual change slightly in the crystal phase of the reflection peaks takes place, which indicates a formation in the crystal phase from BiOBr to α-Bi_2O_3 at different reaction temperature.

3.1.2. SEM–EDS analysis

Bismuth oxybromides were prepared with $Bi(NO_3)_3{\cdot}5H_2O$ and KBr by the hydrothermal method at 110–260 °C for pH = 1–14. The surface morphology of the photocatalysts was examined by FE-SEM–EDS (Figs. 5–7 and Table 3). The FE-SEM image showed that the morphology of the bismuth oxybromides sample obtained at different reaction temperature turned from irregular particles to irregular sheets and plates and then became irregular rods (Fig. 5). Fig. 6 shows that the morphology of the sample obtained at different pH values turned from flower-like crystals to thin sheets and thin plates and then became irregular rods between pH = 1 and pH = 14. Fig. 7 shows that the morphology of the sample obtained at different reaction time turned from sheet-like crystals to thin sheets between 12 h and 36 h. These samples displayed irregular

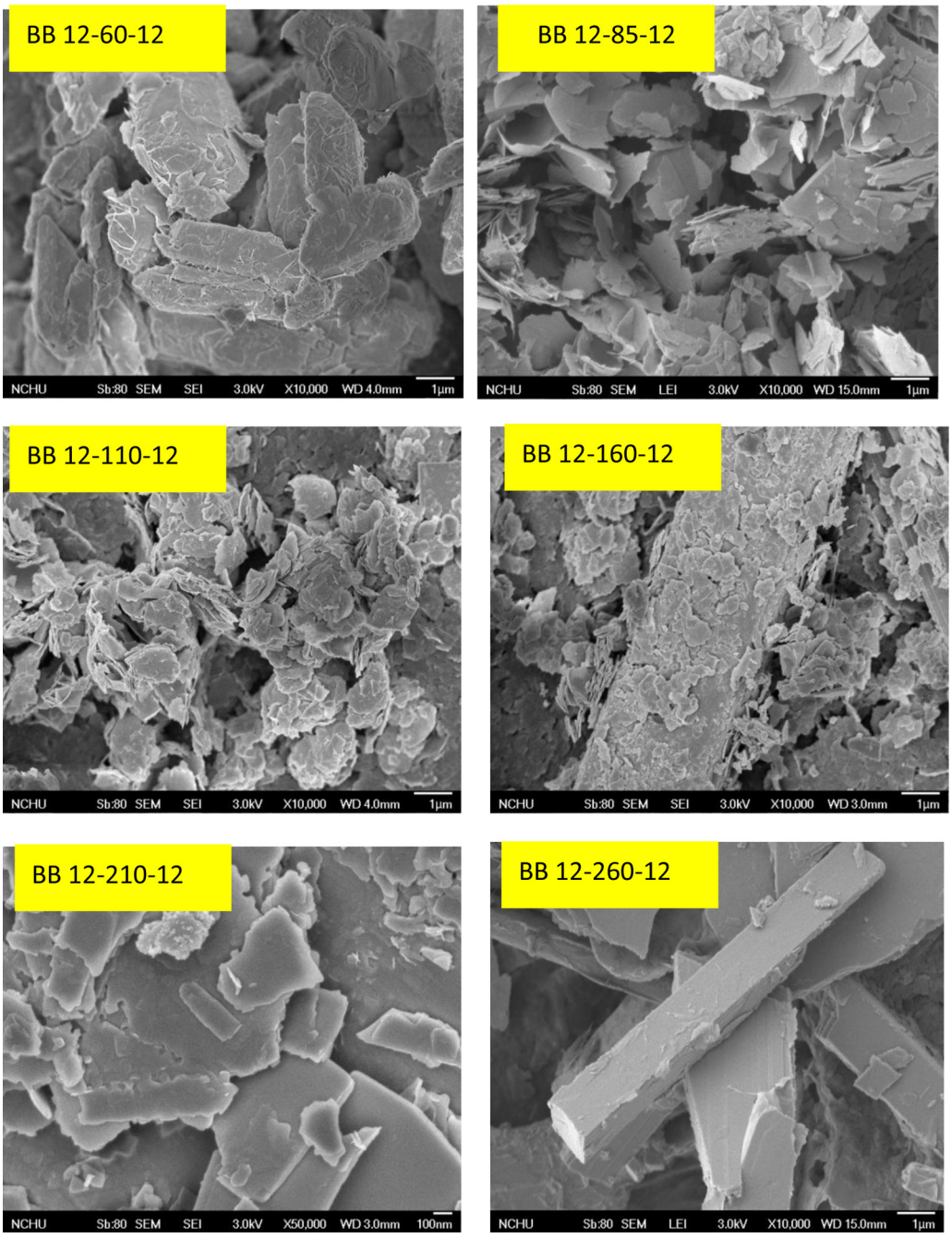

Fig. 5. SEM images of bismuth oxybromide prepared by the hydrothermal autoclave method at different reaction temperature.

nanoplates and nanosheet shapes with a lateral size of several micrometers and a thickness between 5 and 46 nm. Samples BB-13-160-12 and BB-14-160-12 exhibit a rod-like irregular shape with a lateral size of several micrometers. From Table 3, the EDS results showed that the main elements of these samples were bismuth, bromine, and oxygen under different pH values. The Bi/Br atomic ratios of the samples were within the range of 1.07–1680, which corresponded to BiOBr, $Bi_4O_5Br_2$, $Bi_{24}O_{31}Br_{10}$, Bi_3O_4Br, Bi_5O_7Br, $Bi_{12}O_{17}Br_2$, Bi_2O_3 and their mixture phase, compared to the stoichiometric ratio (Bi: Br = 1, 2, 2.4, 3, 5, 6), and could be selectively prepared through a facile solution-based hydrothermal method. The possible processes for the formation of bismuth oxybromides were described as Eqs. (1)–(10).

3.1.3. XPS analysis

XPS is employed to examine the purity of the prepared bismuth oxybromide products, and the spectra are shown in Figs. 8 and 9. The characteristic binding energy value of 157.9 eV for Bi $4f_{7/2}$ (Fig. 8b) revealed a trivalent oxidation state for bismuth. An additional spin–orbit doublet with binding energy of 155.5 eV for Bi $4f_{7/2}$ was also observed in all samples, suggesting that certain parts of bismuth existed in the $(+3-x)$ valence state. This indicated that the trivalent bismuth partially reduced to the lower valence state by the hydrothermal autoclave method. A similar chemical shift of approximately 2.4–2.6 eV for Bi $4f_{7/2}$ was also observed by Jovalekic et al. [35]. They concluded that $Bi^{(+3-x)}$ formal oxidation state could most probably be attributed to the

Table 2
Crystalline phase changes of bismuth oxybromide nanosheets prepared under different pH value and temperature (● BiOBr; ■ $Bi_4O_5Br_2$; ▲ $Bi_{24}O_{31}Br_{10}$; ◆ Bi_3O_4Br; ▼ Bi_5O_7Br; ○ $Bi_{12}O_{17}Br_2$; ★ α-Bi_2O_3).

pH \ Temp	110℃	160℃	210℃	260℃
1	●	●	●■▲◆	●■▲◆
2	●■▲◆	●■▲◆	●■▲◆	●■▲◆
3	●■▲◆	●■▲◆	●■▲◆	●■▲◆
4	●■▲◆	●■▲◆	●■▲◆	●■▲◆
5	●■▲◆	●■▲◆	●■▲◆	●■▲◆
6	●■▲◆	●■▲◆	●■▲◆	●■▲◆
7	●■▲◆	●■▲◆	●■▲◆	●■▲◆
8	●■▲◆	●▲◆	●■▲◆	●■▲◆
9	■◆	■◆	■▲◆	■▲◆
10	■◆	■◆	■◆▼	■◆▼
11	■◆	■◆	■◆▼	■◆▼
12	■◆	■▼○	○▼	○
13	◆	★	★	★
14	★	★	★	★

substoichiometric forms of Bi within the Bi_2O_2 layer, and formation of the low oxidation state resulted in oxygen vacancy in the crystal lattice. However, we assumed that $Bi^{(+3-x)}$ formal oxidation state could most likely be attributed to the substoichiometric forms of Bi at the outer site of the particles, and formation of the low oxidation state resulted in oxygen vacancy in the crystal surface. The binding energy of 68.6 eV and 67.8 eV was referred to the Br $3d_{5/2}$ and $3d_{3/2}$ respectively which can be assigned to the Br at the monovalent oxidation state. Fig. 9 shows the total survey spectra of the Bi 4f, Br 3d, and O 1s XPS of the four bismuth oxybromide samples. According to Fig. 9a, observation of the transition peaks involving the Bi 4f, Br 3d, O 1s, and C 1s orbitals reveals that the catalysts are constituted by elements of C, O, Bi, and Br. In the BB-12-60-12 and BB-9-110-12 samples, only two strong peaks centered at 163.4 and 158.1 eV can be attributed to the Bi $4f_{5/2}$ and Bi $4f_{7/2}$, demonstrating that the main chemical states of the bismuth element in the samples were trivalent. From Table 4, the Bi/Br atomic ratios of the samples were within the range of 1.85–14.29. The XPS result revealed that the possible processes for the formation of bismuth oxybromides were described as Eqs. (1)–(10), which was consistent with the previous result by XRD analysis.

3.1.4. UV–vis diffuse reflectance spectroscopy

The UV–vis adsorption spectra of synthesized catalysts are shown in Fig. 10. Their corresponding band gap energies were calculated, which are close to 2.12–2.76 eV (Tables 3 and 4). Compared to P25, bismuth oxybromides exhibit pronounced light absorbance abilities at $\lambda > 400$ nm, suggesting their potential photocatalytic activity under visible light. The steep shape and strong absorption in the visible region ascribe the visible light

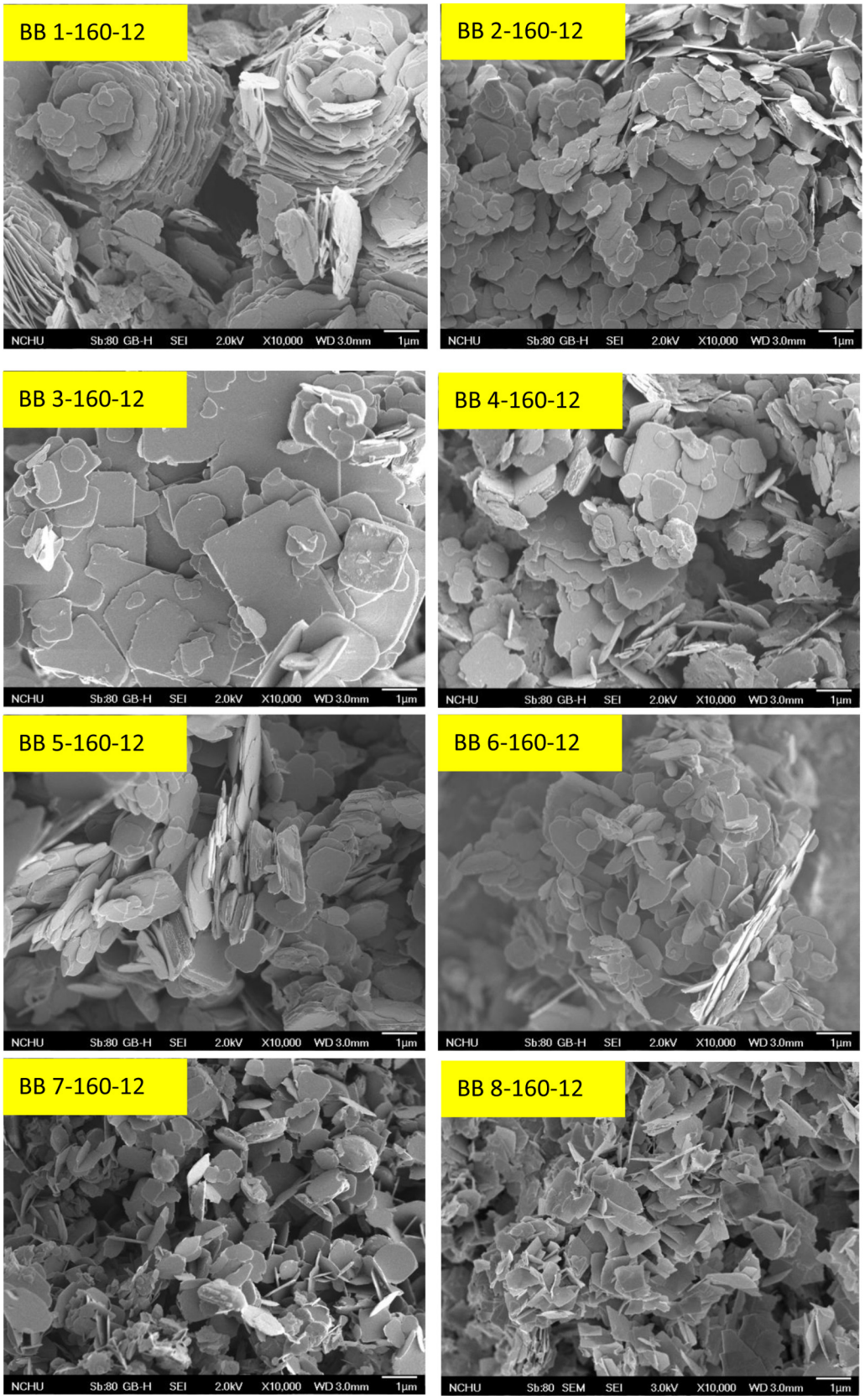

Fig. 6. SEM images of bismuth oxybromide prepared by the hydrothermal autoclave method at different pH value.

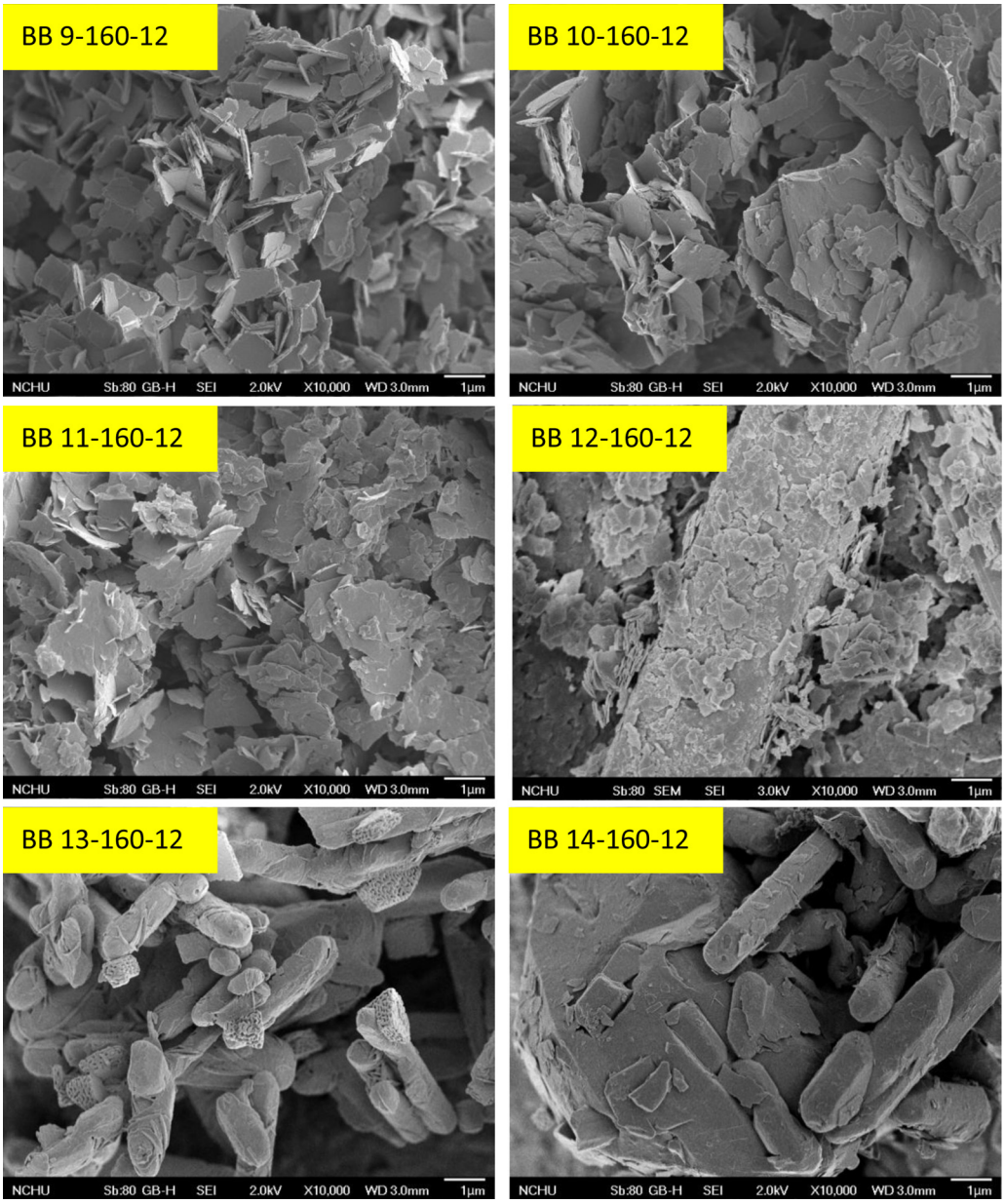

Fig. 6. (*Continued*).

Table 3
Physical and chemical properties of bismuth oxybromides samples by prepared under different pH value.

Catalyst code	pH value	Temp (°C)	Time (h)	EDS atomic ratio (%)			Bi/Br	E_g (eV)	BET (m^2/g)
				Bi	O	Br			
BB 1-160-12	1	160	12	26.85	48.15	25.00	1.07	2.74	4.97
BB 2-160-12	2	160	12	32.88	43.98	23.14	1.42	2.69	4.94
BB 3-160-12	3	160	12	35.57	42.62	21.81	1.63	2.69	2.42
BB 4-160-12	4	160	12	36.99	43.54	19.47	1.90	2.69	3.24
BB 5-160-12	5	160	12	36.38	46.38	17.24	2.11	2.69	2.87
BB 6-160-12	6	160	12	38.58	46.05	15.37	2.51	2.67	4.45
BB 7-160-12	7	160	12	37.78	48.38	13.84	2.73	2.69	4.97
BB 8-160-12	8	160	12	38.44	49.12	12.44	3.09	2.68	9.78
BB 9-160-12	9	160	12	38.34	50.61	11.05	3.47	2.33	5.55
BB 10-160-12	10	160	12	37.99	51.88	10.13	3.75	2.26	5.97
BB 11-160-12	11	160	12	40.45	49.92	9.63	4.20	2.27	4.09
BB 12-160-12	12	160	12	39.22	52.47	8.31	4.72	2.12	4.00
BB 13-160-12	13	160	12	38.85	60.12	1.03	37.72	2.56	0.41
BB 14-160-12	14	160	12	38.64	61.13	0.23	1680	2.54	0.43

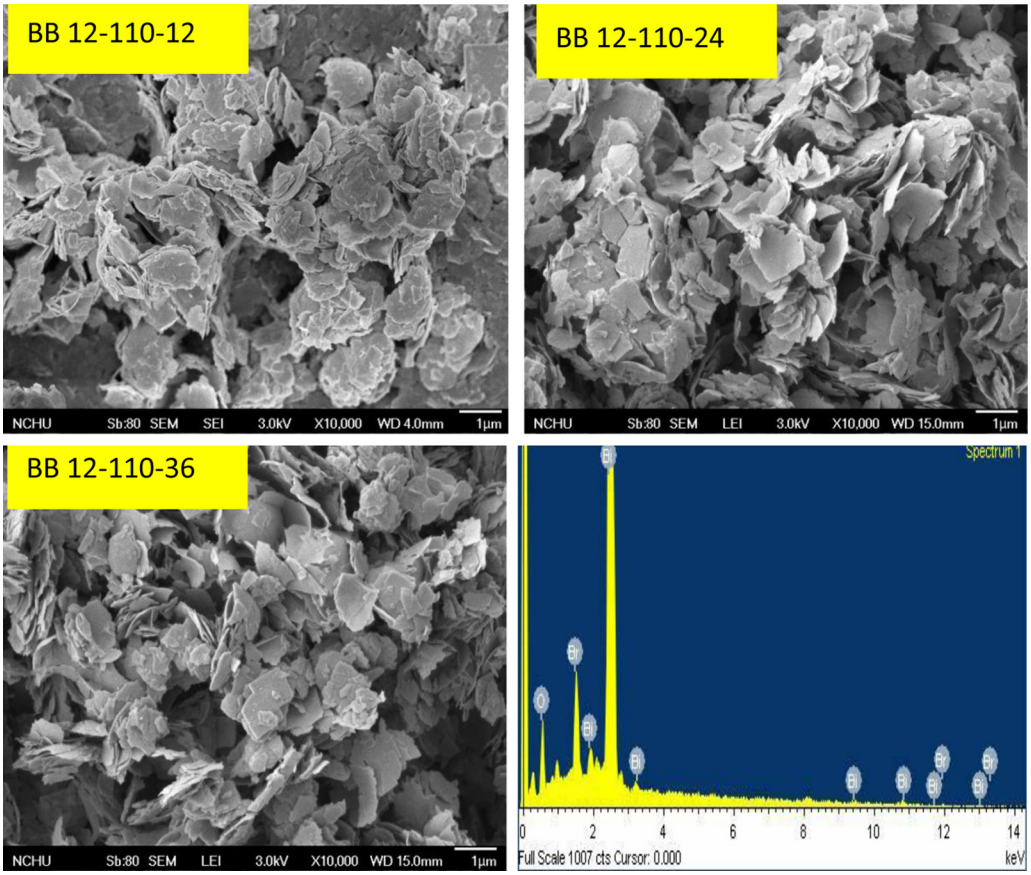

Fig. 7. SEM images and EDS of bismuth oxybromide prepared by the hydrothermal autoclave method at different reaction time.

absorption to the intrinsic band gap transition between the valence band and the conduction band, rather than the transition from the impurity levels [36]. The difference of band gap energy in the prepared bismuth oxybromide can be ascribed to their individual composition with various characteristics.

3.1.5. BET surface areas

From Table 3, The BET of the bismuth oxybromides are about 0.43–9.78 m^2/g, respectively, which is lower than that of P25-TiO_2 with BET of 55.4 m^2/g due to the increased particle size. This nanosheet and nanoplate structure can provide efficient transport paths for reactants and more active sites for the photocatalytic reaction. The structure is also favorable to efficient photo-energy harvesting and introducing the separation of electron–hole pairs, thus promoting the photocatalytic activities.

It is known that the size of nanoparticles has significant effects on the photocatalytic properties due to the variation of surface area, number of active sites and so on [37]. The smaller particle size of nanoparticles would induce to a larger surface area (more active sites) to enhance the photocatalytic activity. Moreover, the band gap energy is also correlated to the photocatalytic activity [38]. The lower band gap has a positive effect on the photocatalytic activity because the lower source energy is needed for arousing a photocatalytic reaction. It means that less energy is needed for activating the nanoparticles to generate excited electron/hole pairs and then induce photocatalytic reactions. In this study, the particle

Table 4
Physical and chemical properties of prepared bismuth oxybromides at different pH value and temperature.

Catalyst code	pH value	Temp (°C)	Time (h)	XPS atomic ratio (%)			Bi/Br	E_g (eV)
				Bi	O	Br		
BB 4-110-12	4	110	12	50.30	36.90	12.80	3.93	2.71
BB 7-110-12	7	110	12	46.40	41.80	11.80	3.93	2.76
BB 9-110-12	9	110	12	47.00	42.90	10.20	4.61	2.30
BB 12-110-12	12	110	12	52.20	40.10	7.80	6.69	2.54
BB 12-60-12	12	60	12	34.30	63.20	2.40	14.29	2.57
BB 12-85-12	12	85	12	42.10	48.10	9.70	4.34	2.28
BB 12-110-12	12	110	12	52.20	40.10	7.80	6.69	2.54
BB 12-160-12	12	160	12	37.10	54.60	8.20	4.52	2.23
BB 12-210-12	12	210	12	38.40	53.30	8.30	4.63	2.26
BB 12-260-12	12	260	12	50.80	41.70	7.50	6.77	2.74
BB 12-110-12	12	110	12	52.20	40.10	7.80	6.69	2.54
BB 12-110-24	12	110	24	48.10	43.00	8.90	5.40	2.22
BB 12-110-36	12	110	36	45.70	45.30	9.00	5.08	2.24

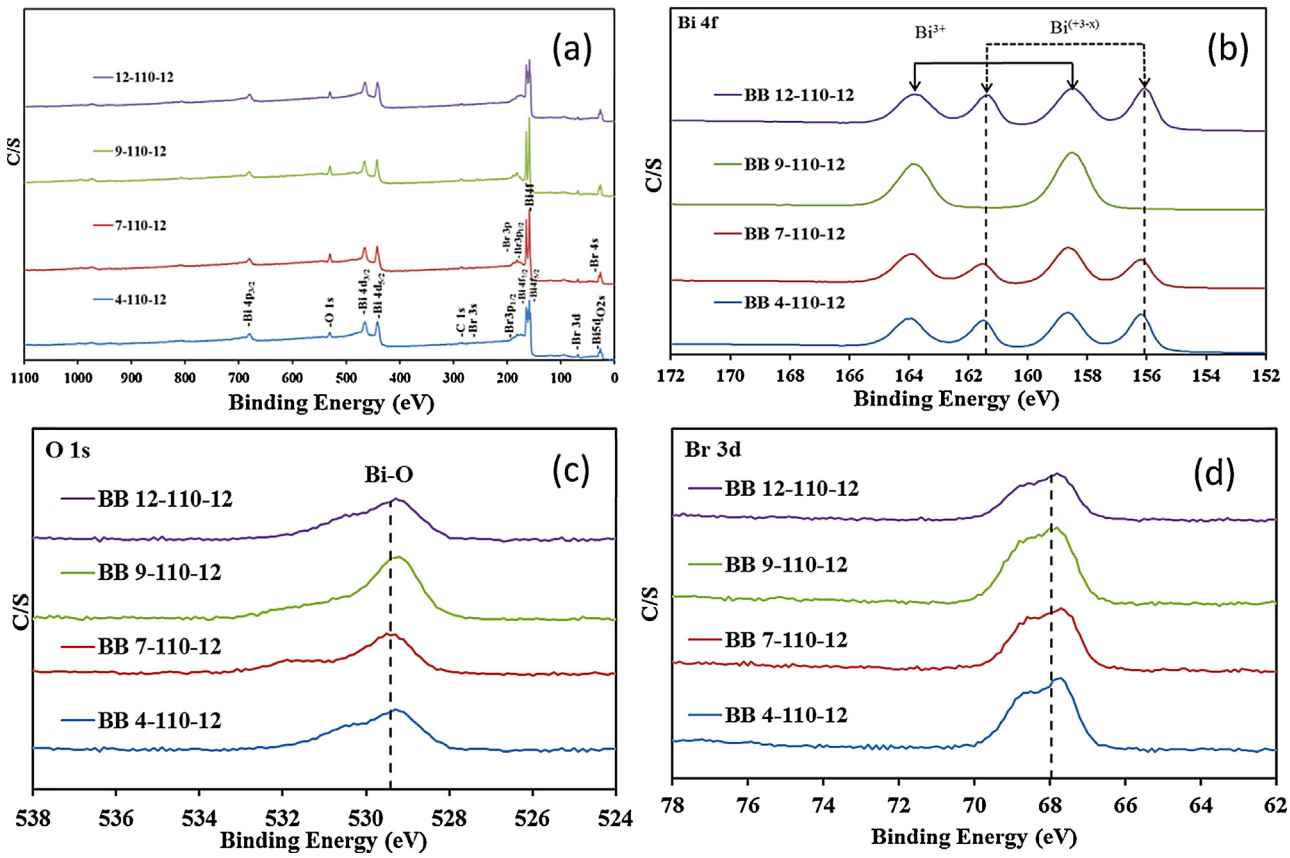

Fig. 8. High-resolution XPS spectra of the bismuth oxybromide prepared by the hydrothermal autoclave method at 110 °C, 12 h, pH = 4, 7, 9, and 12. (a) Total survey; (b) Bi 4f; (c) O 1s; (d) Br 3d.

sizes of bismuth oxybromides were a little higher than those of P25-TiO_2; however, the result of band gap was on the contrary. It suggested that the higher photocatalytic activity of bismuth oxybromides than P25-TiO_2 could be attributed to a lower band gap, which would lead to generate more excited electron–hole pairs to enhance the photocatalytic activity.

3.2. Photocatalytic activity evaluations

3.2.1. Photocatalytic activity

Photocatalytic performance of the bismuth oxybromide catalysts was evaluated by degrading CV under visible light or UV irradiation with 0.5 g/L of catalyst added. The degradation efficiencies as a function of reaction time are illustrated in Figs. 11 and 12. In the absence of catalysts, CV could not be degraded under visible or UV light irradiation. The removal efficiency was enhanced significantly in the presence of bismuth oxybromide catalysts. After 48 h irradiation, bismuth oxybromide showed superior photocatalytic performance, with CV removal efficiency up to 99.9%. The activity of BB-13-110-12 was higher than those of P25-TiO_2, Bi_2WO_6, and $ZnMoO_4$. The superior photocatalytic ability of bismuth oxybromide may be ascribed to its efficient utilization of visible light and the high separation efficiency of the electron–hole pairs with its hieratical structure.

3.2.2. Photoluminescence spectra

To investigate the separation capacity of photogenerated carriers in thin structures, photoluminescence spectra of bismuth oxybromides and P25-TiO_2 are measured and the results are given in Fig. 13. A weak emission peak around 620 nm appears for bismuth oxybromides, which may be derived from the direct electron–hole recombination of band transition. However, the characteristic emission peak around 620 nm nearly disappears for the bismuth oxybromides thin structure, indicating that the recombination of photogenerated charge carriers is inhibited greatly. The efficient charge separation could increase the lifetime of charge carriers and enhance the efficiency of interfacial charge transfer to adsorbed substrates, and then improve the photocatalytic activity.

3.3. Separation and identification of the intermediates

With visible irradiation, temporal variations occurring in the solution of CV dye during the degradation process being examined by HPLC coupled with a photodiode array detector and ESI mass spectrometry. Given the irradiation of CV up to 24 h at pH 4, the chromatograms are illustrated in Fig. 14, and recorded at 580, 350, and 300 nm, and nineteen intermediates were identified, with the retention time under 50 min. The CV dye and its related intermediates were denoted as species **A**–**J**, **a**–**f**, and **α**–**γ**. Except for the initial CV dye (peak A), the peaks initially increased before subsequently decreasing, indicating the formation and transformation of the intermediates.

In Figures S1–S3 of appendix, the maximum absorption of the spectral bands shifted from 585.5 nm (spectrum A) to 543.8 nm (spectrum J), from 377.1 nm (spectrum a) to 342.6 nm (spectrum f), and from 288.3 nm (spectrum **α**) to 274.8 nm (spectrum γ). The maximum adsorption in the visible and ultraviolet spectral region of each intermediate is depicted in Table 5. They were identified as **A**–**J**, **a**–**f**, and **α**–**γ**, respectively corresponding to the peaks **A**–**J**, **a**–**f**, and **α**–**γ** in Fig. 14. These shifts of the absorption band were presumed to result from the formation of a series of

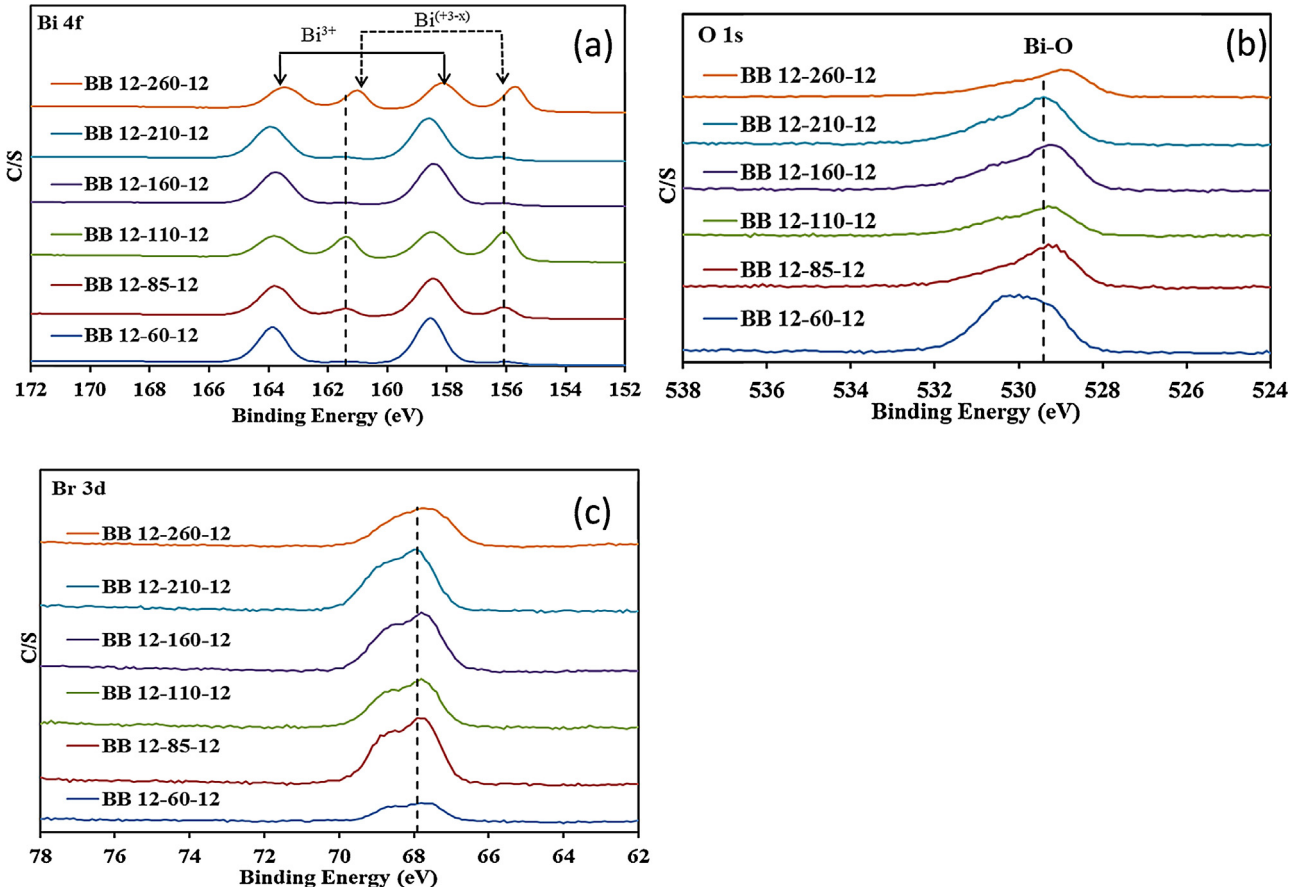

Fig. 9. High-resolution XPS spectra of the bismuth oxybromide prepared by the hydrothermal autoclave method at pH 12, 12 h, temperature = 60, 85, 110, 160, 210, and 260 °C. (a) Bi 4f; (b) O 1s; (c) Br 3d.

N-de-methylated intermediates. From these results, several families of intermediates could be distinguished.

The first family is marked in the chromatogram of Fig. 14a and illustrated in Figure S1(a) for UV–vis absorption spectroscopy. The wavelength position of the major adsorption band of the intermediates of *N*-de-methylated CV dye moved toward the blue region, λ_{max}, **A** (CV), 588.5 nm; **B**, 582.3 nm; **C**, 572.8 nm; **D**, 577.2 nm; **E**, 565.1 nm; **F**, 571.4 nm; **G**, 561.6 nm; **H**, 564.1 nm; **I**, 554.3 nm; **J**, 543.8 nm. The *N*-de-methylation of the CV dye caused the wavelength shifts, depicted in Table 5, due to an attack by one of the active oxygen species on the *N*,*N*-dimethyl or *N*-methyl group. It was previously reported [4] that the CV dye was *N*-de-methylated in a stepwise manner (*i.e.*, methyl groups were removed one by one as confirmed by the gradual peak wavelength shifts toward the blue region) and this was confirmed as Table 5 shown.

Table 5
Intermediates of the photocatalytic degradation of CV identified by HPLC–ESI-MS. Conditions: bismuth oxybromides, 10 mg/L CV, irradiation 24-h.

HPLC peaks	Intermediates	ESI-MS spectrum ions (*m*/*z*)	Absorption maximum (nm)
A	*N*,*N*,*N*′,*N*′,*N*″,*N*″-Hexaethylpararosaniline	372.40	588.5
B	*N*,*N*-Dimethyl-*N*′,*N*′-dimethyl-*N*″-methyl pararosaniline	358.23	582.3
C	*N*,*N*-Dimethyl-*N*′-methyl-*N*″-methylpararosaniline	344.35	572.8
D	*N*,*N*-Dimethyl-*N*′,*N*′-dimethyl pararosaniline	344.23	577.2
E	*N*-Methyl-*N*′-methyl-*N*″-methyl pararosaniline	330.17	565.1
F	*N*,*N*-Dimethyl-*N*′-methylpararosaniline	330.22	571.4
G	*N*-Methyl-*N*′-methylpararosaniline	316.17	561.6
H	*N*,*N*-Dimethylpararosaniline	316.12	564.1
I	*N*-Methylpararosaniline	302.12	554.3
J	Pararosaniline	288.12	543.8
a	4-(*N*,*N*-Dimethylamino)-4′-(*N*′,*N*′-dimethylamino)benzophenone	269.28	377.1
b	4-(*N*,*N*-Dimethylamino)-4′-(*N*′- methylamino)benzophenone	255.23	365.7
c	4-(*N*-Methylamino)-4′-(*N*′-methylamino)benzophenone	241.05	362.9
d	4-(*N*,*N*-Dimethylamino)-4′-aminobenzophenone	241.27	362.3
e	4-(*N*-Methylamino)-4′-aminobenzophenone	227.37	358.9
f	4,4′-Bis-aminobenzophenone	213.30	342.6
α	4-(*N*,*N*-Dimethylamino)phenol	138.08	288.3
β	4-(*N*-Methylamino)phenol	N/A	285.7
γ	4-Aminophenol	N/A	274.8

N/A: Not available.

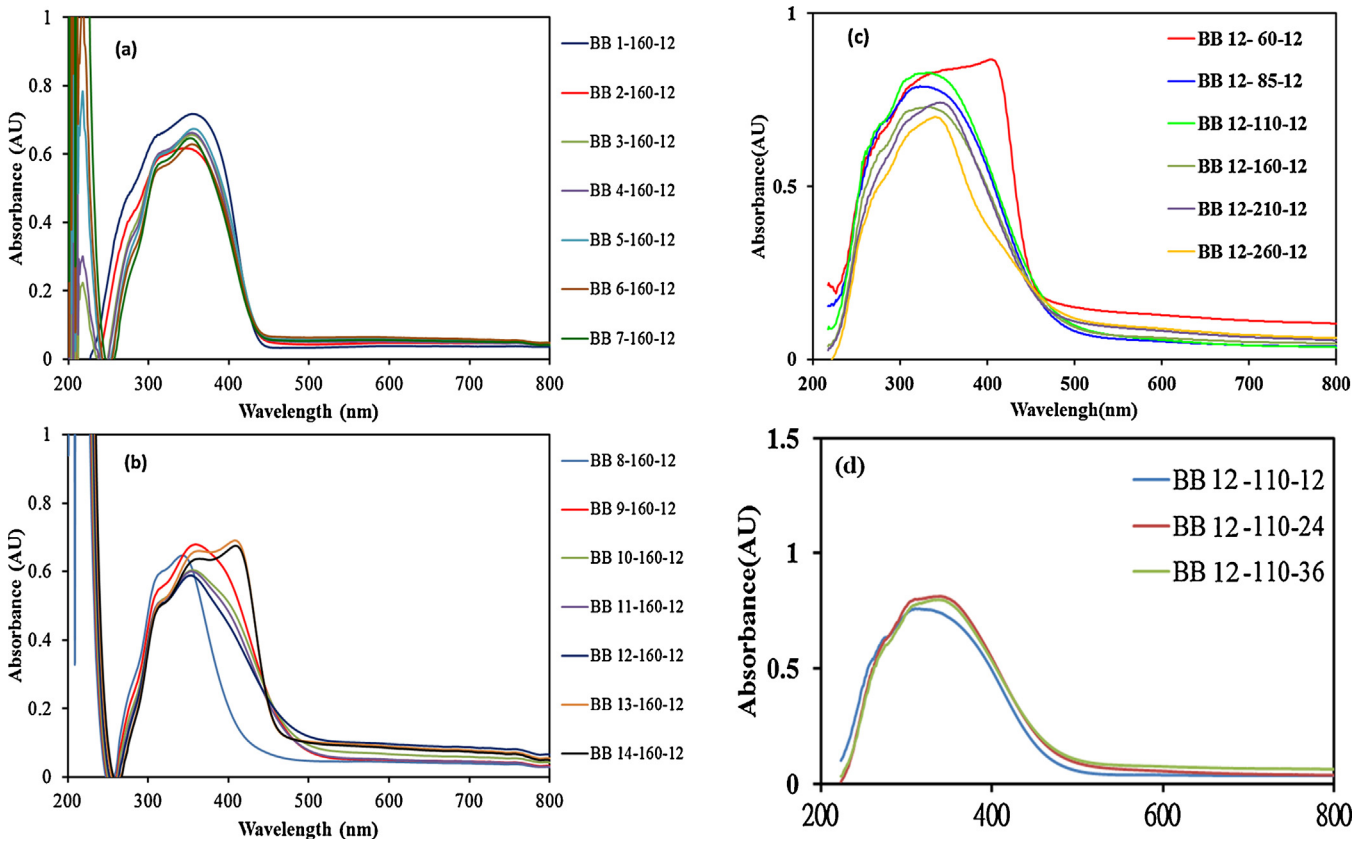

Fig. 10. UV–vis absorption spectra of the prepared bismuth oxybromide catalysts. (a) pH = 1–14; (b) temp = 60–280 °C; (c) time = 12–36 h.

The second family is marked in the chromatogram of Fig. 14b and illustrated in Figure S1(b) for UV–vis absorption spectroscopy. The destruction of CV yielded **a**, **α**, and their *N*-de-methylated products *N*-hydroxymethylated intermediates. The wavelength position of the major adsorption band of the *N*-de-methylation of the **a** and the *N*-hydroxymethylated intermediates of the *N*-de-methylated **a** species, produced by the cleavage of the CV chromophore ring structure, moved toward the blue region, λ_{max}, **a**, 377.1 nm; **b**, 365.7 nm; **c**, 362.9 nm; **d**, 362.3 nm; **e**, 358.9 nm; **f**, 342.6 nm. The proposed intermediate (**a**) was compared with a standard material of 4-(*N*,*N*-dimethylamino)-4′-(*N*′,*N*′-dimethylamino)benzophenone. The retention time and the absorption spectra were identical.

The third family is marked in the chromatogram of Fig. 14c and illustrated in Figure S1(c) for UV–vis absorption spectroscopy. The wavelength position of the major adsorption band of the *N*-de-methylation of the **α**, produced by the cleavage of the CV chromophore ring structure, moved toward the blue region, λ_{max}, **α**, 288.3 nm; **β**, 285.7 nm; **γ**, 274.8 nm. The proposed intermediate (**γ**) was compared with the standard material of 4-aminobenzophenone. The retention time and the absorption spectra were identical.

The intermediates were further identified using the HPLC–ESI mass spectrometric method, and the relevant mass spectra are illustrated in Figure S2 and Table 5. The molecular ion peaks appeared in the acid forms of the intermediates. The results of mass spectral analysis confirmed that the component **A** (CV), *m*/*z* = 372.40, **B**, *m*/*z* = 358.23; **C**, *m*/*z* = 344.35; **D**, *m*/*z* = 344.23; **E**, *m*/*z* = 330.17; **F**, *m*/*z* = 330.22; **G**, *m*/*z* = 316.17; **H**, *m*/*z* = 316.12; **I**, *m*/*z* = 302.12; **J**, *m*/*z* = 288.12; **a**, *m*/*z* = 269.28; **b**, *m*/*z* = 255.23; **c**, *m*/*z* = 241.05; **d**, *m*/*z* = 241.27; **e**, *m*/*z* = 227.37; **f**, *m*/*z* = 213.30; **α**, *m*/*z* = 138.08, in liquid chromatogram.

3.4. Photodegradation mechanisms of CV

Various primary reactive species, such as hydroxyl radical HO•, photogenerated hole h^+, superoxide radical $O_2^{\bullet-}$ and singlet oxygen $^1O_2$, can be formed during the photocatalytic degradation process in the UV–vis/bismuth oxybromide system [16]. Xu et al. investigated that the hydroxyl radicals and direct holes were the primary reactive species in the benzotriazole degradation by BiOBr spheres under simulated solar light irradiation [17]. Ye et al. showed that rhodamine photodegradation by BiOI under visible light was dominated by $O_2^{\bullet-}$ and h^+ oxidation being the main active species [29]. Wang's group revealed that high efficient visible light driven sodium pentachlorophenate removal with Bi_3O_4Br could be attributed to effective separation and transfer of photoinduced charge carriers in Bi_3O_4Br with narrower band gap and more negative conduction band position, which favored the photogenerated electrons trapping with molecular oxygen to produce $O_2^{\bullet-}$ [39]. Ge and Zhang proposed the pathway for generating active oxygen radicals ($O_2^{\bullet-}$ and •OH) on the surface of $In(OH)_xS_y$ for the degradation of RhB [40]. Wang et al. reported that the •OH radical was generated by multistep reduction $O_2^{\bullet-}$ [15]. The generation of $O_2^{\bullet-}$ could not only inhibit the recombination of photoinduced charge carriers, but also benefit the dechlorination of chlorinated phenol derivative. The hydroxyl radical HO• might only be generated via an $e^- \rightarrow O_2^{\bullet-} \rightarrow H_2O_2 \rightarrow$ •OH route. Meanwhile, •OH radical was generated by multistep reduction $O_2^{\bullet-}$ in system. In a valence band of Bi^{3+}, holes formed by photoexcitation are regarded as Bi^{5+} [41]. The standard redox potential of Bi^V/Bi^{III} is more negative than it of $OH^{\bullet}/OH^-$ [42]. Therefore, photogenerated holes on the surface of bismuth oxyhalides are not expected to react with OH^-/H_2O to form •OH, suggesting that the decomposition of bisphenol-A [43] and rhodamine [33] could be attributed to

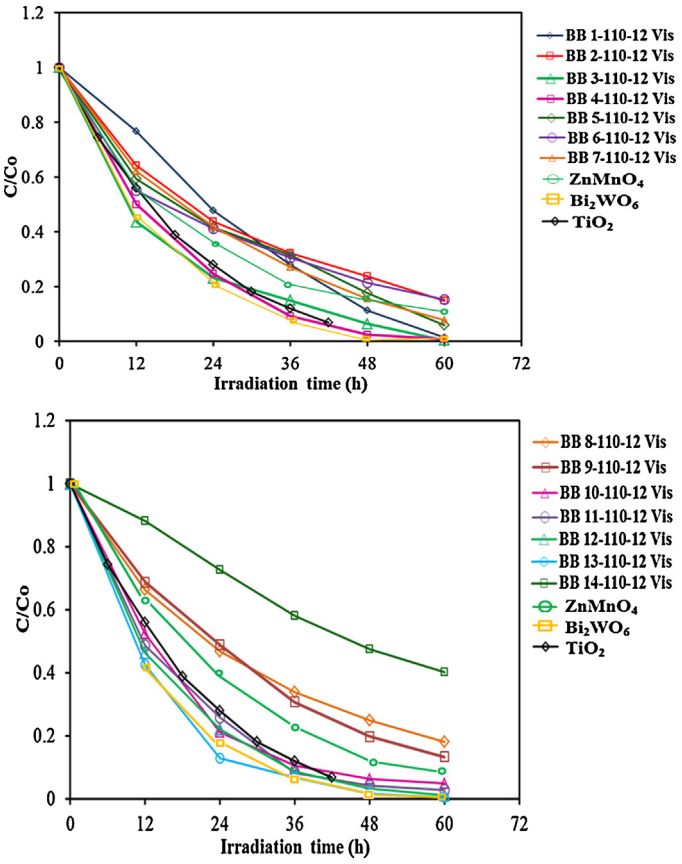

Fig. 11. Photocatalytic degradation of CV by the resulting bismuth oxybromide catalysts and the control experiments under visible light irradiation.

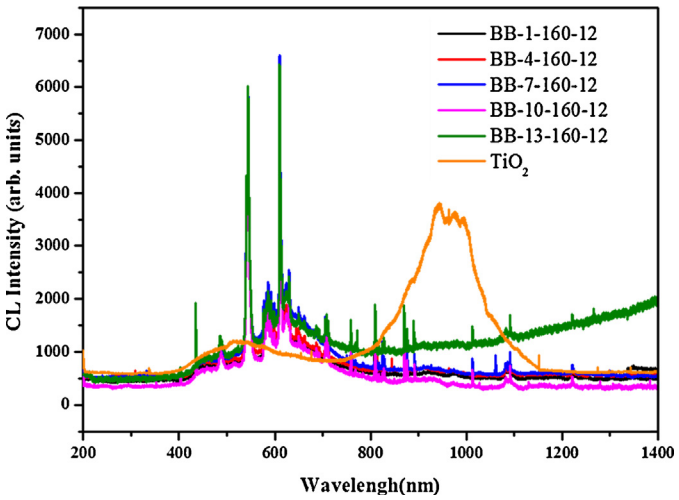

Fig. 13. Photoluminescence spectra of TiO_2 and bismuth oxybromides.

a direct reaction with the photogenerated holes or with superoxide radical (generated by the excited electron) or both species. Zhu et al. reported that photocatalytic experiments in the presence of N_2 and the radical scavenger suggested $^{\bullet}OH$ and $O_2^{\bullet-}$ being two main actives in the whole degradation process [44]. According to previous studies [45,46], the dominant active oxygen species generated in direct oxidation and photocatalytic reactions were $^1O_2$ and $^{\bullet}OH$ radical, respectively. Besides, in this visible light-induced semiconductor system, hydroxylated compounds were also identified for the photocatalytic degradation of CV and Ethyl Violet [47,48]. On the basis of above results and analyses, it is proposed that the probability for the formation of $^{\bullet}OH$ should be much lower than it for $O_2^{\bullet-}$. But, the $^{\bullet}OH$ is an extremely strong, non-selective oxidant, which leads to the partial or complete mineralization of several organic chemicals.

Chen et al. reported [49] that Pt–TiO_2 accumulated less negative species on catalyst surfaces, which deteriorated reaction rates,

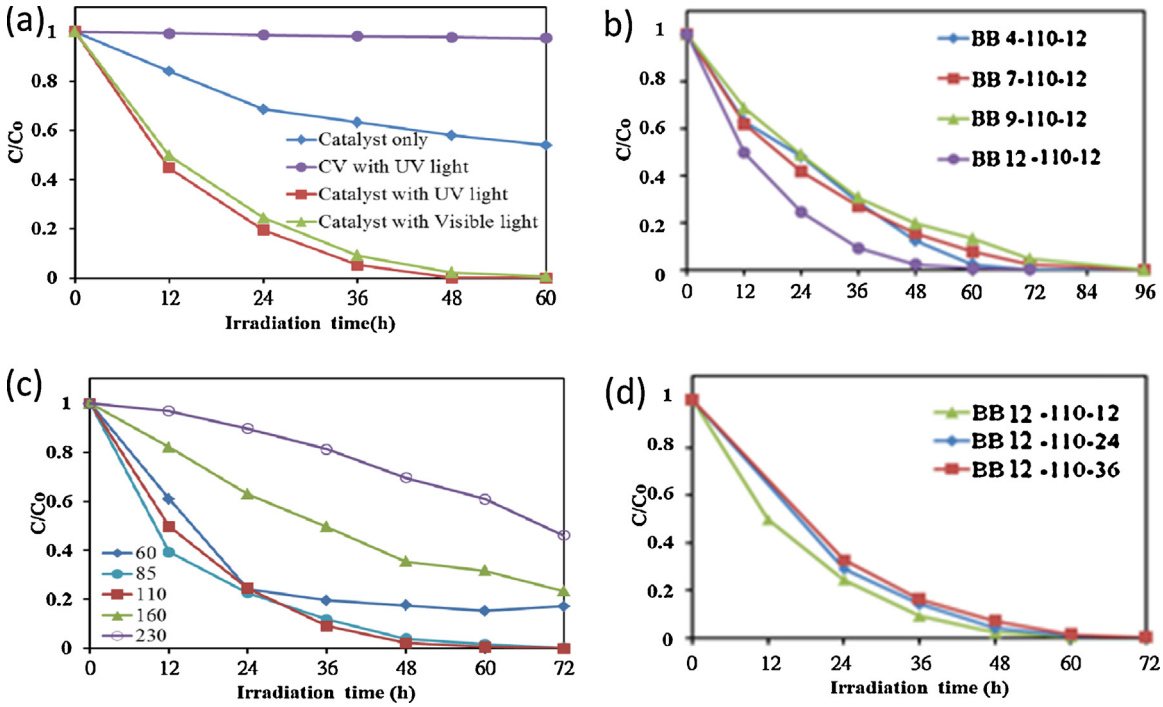

Fig. 12. Photocatalytic degradation of CV by the resulting bismuth oxybromide catalysts and the control experiments under visible light irradiation. (a) pH = ––4; (b) temp = 60–280 °C; (c) time = 12–36 h.

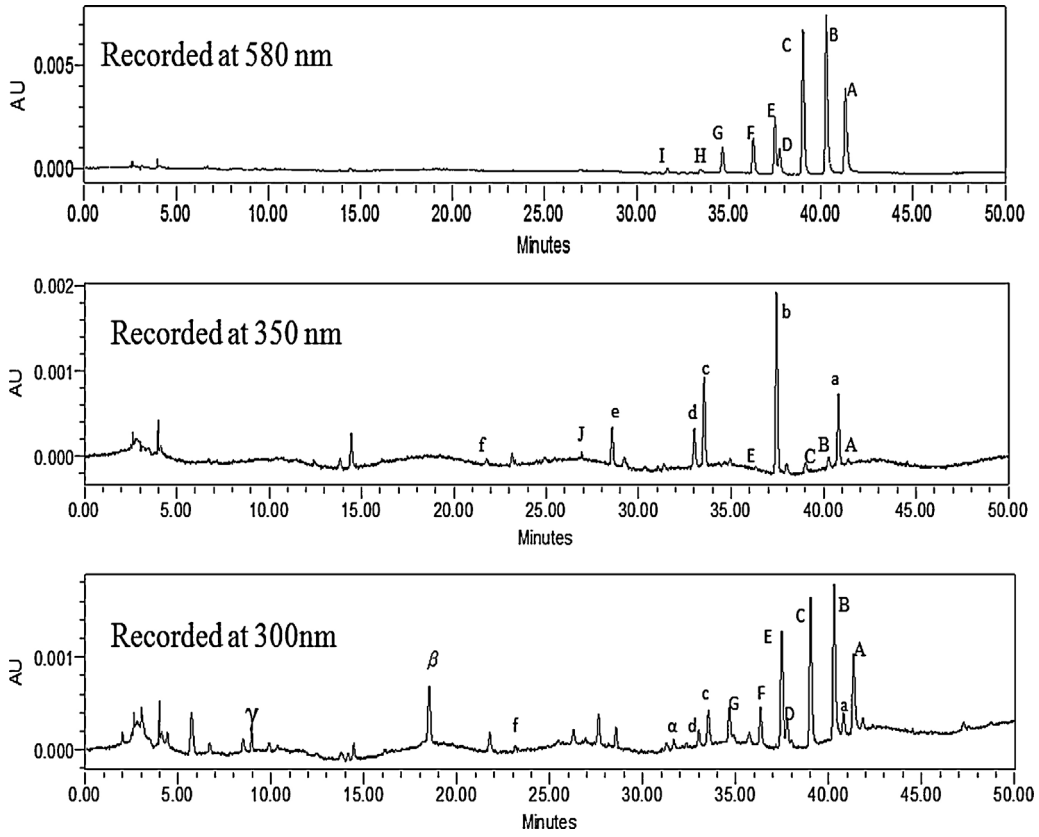

Fig. 14. HPLC chromatogram of the degraded intermediates at different irradiation intervals, recorded at (a) 580 nm, (b) 350 nm, and (c) 300 nm.

than pure TiO_2 did in an acidic environment. The $^{\bullet}OH$ radical is produced subsequently, as also shown in Eqs. (11)–(14).

$$O_2^{\bullet-} + H^+ + e^- \rightarrow HOO^{\bullet} \quad (11)$$

$$HOO^{\bullet} + H_2O \rightarrow {}^{\bullet}OH + H_2O_2 \quad (12)$$

$$O_2^{\bullet-} + 2H^+ \rightarrow H_2O_2 \quad (13)$$

$$H_2O_2 + e^- \rightarrow {}^{\bullet}OH + OH^- \quad (14)$$

These cycles continuously occur when the system is exposed to the visible light irradiation. Finally, after several cycles of photo-oxidation, the degradation of CV by the formed oxidant species can be expressed by Eqs. (15) and (16):

$$CV + OH^{\bullet} \rightarrow \text{degradedcompounds} \quad (15)$$

$$CV^{\bullet+} + OH^{\bullet} \rightarrow \text{degradedcompounds} \quad (16)$$

It has been reported that dye exhibits a mechanisms of dye sensitized degradation [44,50,51]. This photocatalytic degradation is also attributed to the photodegradation of CV through the photocatalytic pathway of CV photosensitized bismuth oxybromide. CV absorbing a visible photon is promoted to an excited electronic state CV*, from which an electron can be transferred into the conduction band of bismuth oxybromide:

$$CV + h\nu \rightarrow CV* \quad (17)$$

$$CV* + \text{bismuthoxybromide} \rightarrow CV^+ + \text{bismuthoxybromide}(e^-) \quad (18)$$

$$O_2 + e^- \rightarrow O_2^{\bullet-} \quad (19)$$

Once the electron reaches the bismuth oxybromide conduction band, it subsequently induces the generation of active oxygen species (Eqs. (19) and (11)–(14)), which result in the degradation of CV. Clearly, apart from the photodegradation of CV through the photocatalytic pathway of CV-photosensitized bismuth oxybromide, there is another kind of photocatalytic pathway to account for the enhanced photocatalytic activity.

In earlier reports [49,52], the *N*-de-alkylation processes were preceded by the formation of a nitrogen-centered radical while the oxidative degradation (destruction of dye chromophore structures) was preceded by the generation of a carbon-centered radical in the photocatalytic degradation of triphenylmethane dye. On the basis of the above experimental results, the dye degradation mechanism is tentatively proposed, depicted in Fig. 15. The excited dye injects an electron into the conduction band of bismuth oxybromide, where it is scavenged by O_2 to form $O_2^{\bullet-}$. De-methylation of CV dye occurs mostly through attack by the active species, which is a perfect nucleophilic reagent, on the *N*-methyl portion of CV. Further, $O_2^{\bullet-}$ subsequently reacts with H_2O to generate $^{\bullet}OH$ radical and the other active radical. The probability for the formation of $^{\bullet}OH$ should be much lower than that for $O_2^{\bullet-}$. The $^{\bullet}OH$ is an extremely strong, non-selective oxidant, which leads to the partial or complete mineralization of several organic chemicals. All the above active radicals drive the photodegradation or mineralization of the dye molecule. Under visible light irradiation, all the intermediates identified in these two studied topics have the same result. There is no doubt that the major oxidant is $^{\bullet}OH$ radical, not $O_2^{\bullet-}$.

During the initial period of CV dye photodegradation by bismuth oxybromide, competitive reactions between *N*-de-methylation and oxidative degradation occurs based on the intermediates identified. The detailed mechanisms are illustrated in Figures S3 and S4. The first pathway involves a hydroxyl radical attack on the *N*,*N*-methylamino group of CV, resulting in a reactive cationic radical, the subsequent de-methylation and oxidation of which eventually yield the first group intermediates. The results

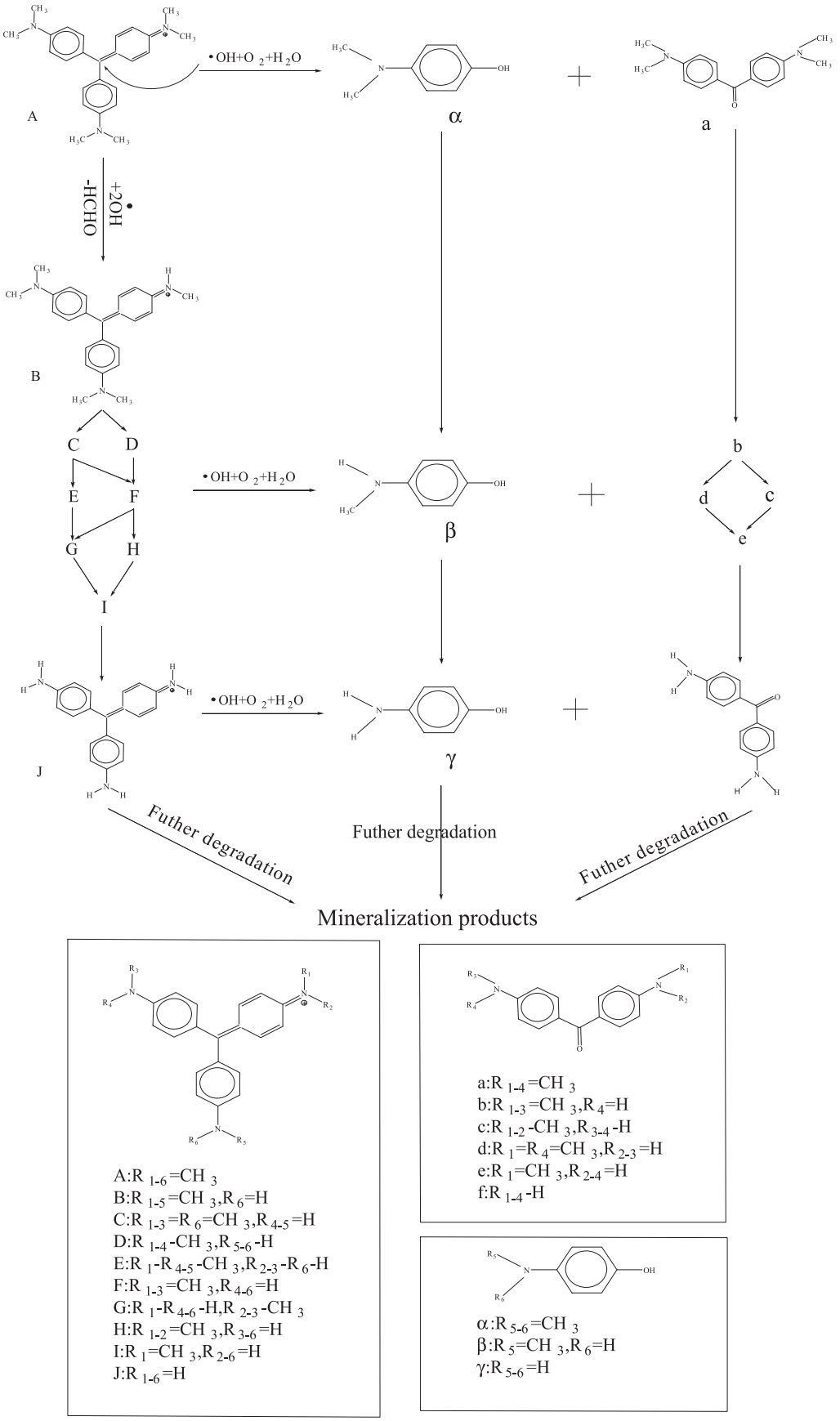

Fig. 15. Proposed photodegradation mechanism of the CV dye.

indicated that the *N*-de-methylation degradation of CV dye took place in a stepwise manner to yield mono-, di-, tri-, tetra-, penta-, hexa-*N*-de-methylated CV species during the process.

The second pathway involves a hydroxyl radical attack on the central carbon atom of CV, yielding a reactive cationic radical, with a bond between the central carbon atom and the *N*,*N*-dimethylamino phenyl ring that is cleaved to give one set of intermediates **a** and **α**. In addition, these intermediates can further be attacked by hydroxyl radicals, giving a reactive cationic radical which is demethylated, resulting in **f** and **γ**. The latter intermediates are further oxidized to form mineralization products.

4. Conclusion

Bismuth oxybromides were synthesized by a facile hydrothermal method with $Bi(NO_3)_3$ and KBr as the Bi and Br source. In the current process, the controllable crystal phases and morphologies of bismuth oxybromide could be achieved by simply changing some growth parameters, including pH and temperature. Normally, BiOBr was acquired at pH ≦ 8 and pure phase BiOBr at pH = 1, temp = 110–160 °C; $Bi_4O_5Br_2$ between pH ≧ 1, temp ≧ 210 °C and pH ≦ 12, temp ≦ 160 °C; $Bi_{24}O_{31}Br_{10}$ between pH ≧ 1, temp ≧ 210 °C and pH ≦ 9, temp ≧ 210 °C; Bi_3O_4Br between pH ≦ 1, temp ≧ 210 °C and pH ≦ 12, temp ≦ 110 °C and pure phase Bi_3O_4Br at pH = 13, temp = 110 °C; Bi_5O_7Br between pH ≧ 10, temp ≧ 210 °C and pH ≦ 12, temp ≦ 210 °C; $Bi_{12}O_{17}Br_2$ at pH = 2 and 160 °C ≦ temp ≦ 260 °C and pure phase $Bi_{12}O_{17}Br_2$ at 260 °C; and, Bi_2O_3 microstructures at higher base concentration (pH ≧ 13) in the synthetic conditions. The prepared bismuth oxybromide catalysts were of different phases, which removed nearly 100% of CV from the solution after 48 h under visible light irradiation, and the high photoactivity can be attributed to their relatively efficient utilization of visible light. Removal efficiencies demonstrated the superior photocatalytic ability of bismuth oxybromide. With the bismuth oxybromides as the catalyst, both *N*-de-methylation and conjugated structure of CV dye took place during the degradation process. The reaction mechanisms for vis/bismuth oxybromides proposed in this study should offer some insight for the future development of technology applications to the decoloration of dyes.

Acknowledgment

This research was supported by the National Science Council of the Republic of China.

Appendix A. Supplementary data

Supplementary data associated with this article can be found, in the online version, at http://dx.doi.org/10.1016/j.jtice.2013.12.015.

References

[1] Malato S, Fernández-Ibáñez P, Maldonado MI, Blanco J, Gernjak W. Decontamination and disinfection of water by solar photocatalysis: recent overview and trends. Catal Today 2009;147:1–59.
[2] Shannon MA, Bohn PW, Elimelech M, Georgiadis JG, Marinas BJ, Mayes AM. Science and technology for water purification in the coming decades. Nature 2008;452:301–10.
[3] Khan S, Al-Shahry M, Ingler JWB. Efficient photochemical water splitting by a chemically modified n-TiO_2. Science 2002;297:2243–5.
[4] Liao YHB, Wang JX, Lin JS, Chung WH, Lin WY, Chen CC. Synthesis,photocatalytic activities and degradation mechanism of Bi_2WO_6 toward crystal violet. Catal Today 2011;174:148–59.
[5] Ren J, Wang W, Shang M, Sun S, Gao E. Heterostructured bismuth molybdate composite: preparation and improved photocatalytic activity under visible-light irradiation. ACS Appl Mater Interfaces 2011;3:2529–33.
[6] Wang D, Li R, Zhu J, Shi J, Han J, Zong X, et al. Photocatalytic water oxidation on $BiVO_4$ with the electrocatalyst as an oxidation cocatalyst: essential relations between electrocatalyst and photocatalyst. J Phys Chem C 2012;116:5082–9.
[7] Casbeer E, Sharma VK, Li XZ. Synthesis and photocatalytic activity of ferrites under visible light: a review. Sep Purif Technol 2012;87:1–14.
[8] Kudo A, Omori K, Kato H. A novel aqueous process for preparation of crystal form-controlled and highly crystalline $BiVO_4$ powder from layered vanadates at room temperature and its photocatalytic and photophysical properties. J Am Chem Soc 1999;121:11459–67.
[9] Lee WW, Chung WH, Huang WS, Lin WC, Lin WY, Jiang YR, et al. Photocatalytic activity and mechanism of nano-cubic barium titanate prepared by a hydrothermal method. J Taiwan Inst Chem Eng 2013;44:660–9.
[10] Chen Z, Wang W, Zhang Z, Fang X. High-efficiency visible-light-driven Ag_3PO_4/AgI photocatalysts: Z-scheme photocatalytic mechanism for their enhanced photocatalytic activity. J Phys Chem C 2013;117:19346–52.
[11] Wang RC, Fan KS, Chang JS. Removal of acid dye by $ZnFe_2O_4$/TiO_2-immobilized granular activated carbon under visible light irradiation in a recycle liquid–solid fluidized bed. J Taiwan Inst Chem Eng 2009;40:533–40.
[12] Xu J, Meng W, Zhang Y, Li L, Guo C. Photocatalytic degradation of tetrabromobisphenol a by mesoporous BiOBr: efficacy, products and pathway. Appl Catal B 2011;107:355–62.
[13] Huo Y, Zhang J, Miao M, Jin Y. Solvothermal synthesis of flower-like BiOBr microspheres with highly visible-light photocatalytic performances. Appl Catal B: Environ 2012;111/112:334–41.
[14] Yu C, Zhou W, Yu J, Cao F, Li X. Thermal stability, microstructure and photocatalytic activity of the bismuth oxybromide photocatalyst. Chin J Chem 2012;30:721–6.
[15] Wang J, Yu Y, Zhang L. Highly efficient photocatalytic removal of sodium pentachlorophenate with Bi_3O_4Br under visible light. Appl Catal B: Environ 2013;136/137:112–21.
[16] Xiao X, Hu R, Liu C, Xing C, Zuo X, Nan J, et al. Facile microwave synthesis of novel hierarchical $Bi_{24}O_{31}Br_{10}$ nanoflakes with excellent visible light photocatalytic performance for the degradation of tetracycline hydrochloride. Chem Eng J 2013;225:790–7.
[17] Xu J, Li L, Guo CS, Zhang Y, Wang SF. Removal of benzotriazole from solution by BiOBr photocatalysis under simulated solar irradiation. Chem Eng J 2013;221:230–7.
[18] Xia J, Yin S, Li H, Xu H, Xu L, Xu Y. Improved visible light photocatalytic activity of sphere-like BiOBr hollow and porous structures synthesized via a reactable ionic liquid. Dalton Trans 2011;40:5249–58.
[19] Fang YF, Huang YP, Yang J, Wang P, Cheng GW. Unique ability of BiOBr to decarboxylate D-Glu and D-MeAsp in the photocatalytic degradation of microcystin-LR in water. Environ Sci Technol 2011;45:1593–600.
[20] Deng H, Wang J, Penng Q, Wang X, Li Y. Controlled hydrothermal synthesis of bismuth oxyhalide nanobelts and nanotubes. Chem Eur J 2005;11:6519–24.
[21] Ullmann's encyclopedia of industrial chemistry. Part A27. Triarylmethane and diarylmethane dyes. 6th ed. New York: Wiley-VCH; 2001.
[22] Duxbury DF. The photochemistry and photophysics of triphenylmethane dyes in solid and liquid media. Chem Rev 1993;93:381–433.
[23] Inoue T, Kikuchi K, Hirose K, Iiono M, Nagano T. Small molecule-based laser inactivation of inositol 1,4,5-trisphosphate receptor. Chem Biol 2001;8:9–15.
[24] Green FJ. The Sigma–Aldrich handbook of stains, dyes, and indicators. Milwaukee, WI: Aldrich Chemical; 1990, 766 pp..
[25] Geethakrishnan T, Palanisamy PK. Degenerate four-wave mixing experiments in Methyl green dye-doped gelatin film. Optik 2006;117:282–6.
[26] Nakane H, Ono K. Differential inhibitory effects of some catechin derivatives on the activities of human immunodeficiency virus reverse transcriptase and cellular deoxyribonucleic and ribonucleic acid polymerases. Biochemistry 1990;29:2841–5.
[27] Bonnett R, Martinez G. Photobleaching of sensitisers used in photodynamic therapy. Tetrahedron 2001;57:9513–47.
[28] Cho BP, Yang T, Blankenship LR, Moody JD, Churchwell M, Bebland FA, et al. Synthesis and characterization of *N*-demethylated metabolites of malachite green and leucomalachite green. Chem Res Toxicol 2003;16:285–94.
[29] Ye L, Chen J, Tian L, Liu J, Peng T, Deng K, et al. BiOI thin film via chemical vapor transport: photocatalytic activity, durability, selectivity and mechanism. Appl Catal B: Environ 2013;130/131:1–7.
[30] Xiao X, Zhang WD. Hierarchical $Bi_7O_9I_3$ micro/nano-architecture: facile synthesis, growth mechanism, and high visible light photocatalytic performance. RSC Adv 2011;1:1099–105.
[31] Sun S, Wang W, Zhang L, Ahou L, Yin W, Shang M. Visible light-induced efficient contaminant removal by Bi_5O_7I. Environ Sci Technol 2009;43:2005–10.
[32] Ye L, Tian L, Peng T, Zan L. Synthesis of highly symmetrical BiOI single-crystal nanosheets and their {0 0 1} facet-dependent photoactivity. J Mater Chem 2011;21:12479–84.
[33] Sanaa SK, Vladimir U, Sveta F, Inna P, Yoel S. A novel class of heterojunction photocatalysts with highly enhanced visible light photocatalytic performances: yBiO(Cl_xBr_{1-x})-$(1-y)$ bismuth oxide hydrate. Appl Catal B: Environ 2012;117/118:148–55.
[34] Kong L, Jiang Z, Lai HH, Nicholls RJ, Xiao T, Jones MO, et al. Unusual reactivity of visible-light-responsive AgBr–BiOBr heterojunction photocatalysts. J Catal 2012;293:116–25.
[35] Jovalekic C, Pavlovic M, Osmokrovic P, Atanasoska L. X-ray photoelectron spectroscopy study of $Bi_4Ti_3O_{12}$ ferroelectric ceramics. Appl Phys Lett 1998;72:1051–3.

[36] Zhang J, Shi F, Lin J, Chen D, Gao J, Huang Z, et al. Self-assembled 3-D architectures of BiOBr as a visible light-driven photocatalyst. Chem Mater 2008;20:2937–41.
[37] Lin WC, Yang WD, Jheng SY. Photocatalytic degradation of dyes in water using porous nanocrystalline titanium dioxide. J Taiwan Inst Chem Eng 2012; 43:269–74.
[38] Manna L, Scher EC, Alivisatos AP. Shape control of colloidal semiconductor nanocrystals. J Cluster Sci 2002;13:521–32.
[39] Wang J, Yu Y, Zhang L. Highly efficient photocatalytic removal of sodium pentachlorophenate with Bi_3O_4Br under isible light. Appl Catal B: Environ 2013;136/137:112–21.
[40] Ge S, Zhang L. Efficient visible light driven photocatalytic removal of RhB and NO with low temperature synthesized $In(OH)_xS_y$ hollow nanocubes: a comparative study. Environ Sci Technol 2011;45:3027–33.
[41] Fu H, Pan C, Yao W, Zhu Y. Visible-light-induced degradation of rhodamine B by nanosized Bi_2WO_6. J Phys Chem B 2005;109:22432–39.
[42] Kim S, Choi W. Kinetics and mechanisms of photocatalytic degradation of $(CH_3)_nNH_{4-n}^+$ $(0 \le n \le 4)$ in TiO_2 suspension: the role of OH radicals. Environ Sci Technol 2002;36:2019–25.
[43] Xiao X, Hao R, Liang M, Zuo X, Nan J, Li L, et al. One-pot solvothermal synthesis of three-dimensional (3D) BiOI/BiOCl composites with enhanced visible-light photocatalytic activities for the degradation of bisphenol-A. J Hazard Mater 2012;233/234:122–30.
[44] Zhu X, Zhang J, Chen F. Studt on visible light photocatalytic activity and mechanism of spferical $Bi_{12}TiO_{20}$ nanoparticles prepared by low-powder hydrothermal method. Appl Catal B: Environ 2011;102:316–22.
[45] Yu K, Yang S, Liu C, Chen H, Li H, Sun C, et al. Degradation of organic dyes via bismuth silver oxide initiated direct oxidation coupled with sodium bismuthate based visible light photocatalysis. Environ Sci Technol 2012;46: 7318–26.
[46] Yu K, Yang S, Boyd SA, Chen H, Sun C. Efficient degradation of organic dyes by $BiAg_xO_y$. J Hazard Mater 2011;197:88–96.
[47] Lee WW, Lin JS, Chang JL, Chen JY, Cheng MC, Chen CC. Photodegradation of CV over nanocrystalline bismuth tungstate prepared by hydrothermal synthesis. J Mol Catal A: Chem 2012;361/362:80–90.
[48] Mai FD, Liu CS, Chen JL, Chen CC. Photodegradation of methyl green using visible irradiation in ZnO suspensions. Determination of the reaction pathway and identification of intermediates by a high-performance liquid chromatography–photodiode array–electrospray ionization-mass spectrometry method. J Chromatogr A 2008;1189:355–65.
[49] Fan HJ, Lu CS, Lee WLW, Chiou MR, Chen CC. Mechanistic pathways differences between P25-TiO_2 and Pt–TiO_2 mediated CV photodegradation. J Hazard Mater 2011;185:227–35.
[50] Li Y, Zhang H, Hu X, Zhao X, Han M. Efficient visible-light-induced photocatalytic activity of a 3D-ordered titania hybrid photocatalyst with a core/shell structure of dye-containing polymer/titania. J Phys Chem C 2008;112:14973–79.
[51] Zhu X, Zhang J, Chen F. Study on visible light photocatalytic activity and mechanism of spherical $Bi_{12}TiO_{20}$ nanoparticles prepared by low-power hydrothermal method. Appl Catal B: Environ 2011;102:316–22.
[52] Lee WLW, Huang ST, Chang JL, Chen JY, Cheng MC, Chen CC. Photodegradation of CV over nanocrystalline bismuth tungstate prepared by hydrothermal synthesis. J Mol Catal A: Chem 2012;361/362:80–90.